Metamaterial-enabled wireless and contactless ultrasonic power transfer and data transmission through a metallic wall

Jun Ji, Hyeonu Heo, Jiaxin Zhong, Mourad Oudich, Yun Jing

Metamaterial-enabled wireless and contactless ultrasonic power transfer and data transmission through a metallic wall

Jun Ji,[1,*] Hyeonu Heo,[1,*] Jiaxin Zhong,[1,*] Mourad Oudich,[1,2,†] and Yun Jing[1,‡]

[1] *Graduate Program in Acoustics, The Pennsylvania State University, University Park, Pennsylvania, 16802, USA*
[2] *Université de Lorraine, CNRS, Institut Jean Lamour, F-54000 Nancy, France*

(Dated: December 15, 2023)

Wireless ultrasonic power transfer and data transmission through a metallic wall requires a direct contact of transducers with the wall owing to the significant impedance mismatch between the surrounding fluid and the wall. Here, a pillar-based acoustic metamaterial is proposed for wireless and contactless ultrasonic power transfer and data transmission through a metallic wall by leveraging the pillar's vertical elongation mode. Experiments conducted in water demonstrate a 33-fold power transmission enhancement (from 2% to around 66%) at approximately 450 kHz through a 1 mm thick metallic wall. Furthermore, our experiments show that a commercial light-emitting diode can be illuminated by harvesting the metamaterial-enhanced transmission of ultrasonic energy, which would not have been possible with the metallic wall alone even at an input voltage approximately five times greater. In addition, data transmission through the metallic wall is demonstrated by employing amplitude shift keying modulation to transmit an image, showcasing the remarkable improvement in image quality enabled by the metamaterial. This study paves the way for a future generation of wireless and contactless ultrasonic power transfer and data transmission applications.

INTRODUCTION

Wireless ultrasonic power transfer (W-UPT) and data transmission (W-UDT) through a metallic wall is an exciting and rapidly advancing field of research, as metal barriers typically hinder the use of electromagnetic power transfer due to the Faraday shielding effect [1–3]. Based upon such technologies, sensors and actuators enclosed in hermetical metal containers can be wirelessly powered and can communicate with exterior environments through intact metal walls, benefiting a variety of applications in aeronautic and aerospace engineering [4, 5] and nuclear engineering [6, 7]. Conventionally, W-UPT and W-UDT utilize at least a pair of PZT (Lead zirconate titanate) ultrasound transducers attached to a metal barrier. The main limitation of this approach, however, is that it requires direct contact of piezoelectric transducers with metal walls using couplants to ensure a good acoustic transmission path. The quality of couplants, such as epoxy, may degrade or even fail as operating time goes by [1], which can introduce large impedance mismatch over the acoustic-electric channel and cause the power transfer and data transmission efficiency to rapidly decrease. Therefore, wireless and contactless ultrasonic power transfer (WC-UPT) and data transmission (WC-UDT) through a metallic wall is highly desirable.

Meanwhile, acoustic metamaterials [8] have attracted numerous research efforts in recent years due to their capability to control the propagation of sound in unconventional ways, which have led to interesting phenomena and applications such as cloaking [9–11], sub-wavelength imaging [12–14], and unidirectional transparency [15, 16]. Despite significant advancements in acoustic metamaterials, a demonstration of an acoustic metamaterial capable of facilitating WC-UPT and WC-UDT through a metallic wall has yet to be achieved. On the one hand, whereas extraordinary acoustic transmission has been enabled by near-zero-density metamaterials [17, 18] and acoustic evanescent waves [19–22], these designs still require small apertures for sound transmission, defeating the purpose of W-UPT and W-UDT. On the other hand, complementary acoustic metamaterials [23–25] have been theoretically proposed to achieve enhanced transmission non-invasively through an impedance-mismatched layer, utilizing doubly negative acoustic properties. However, experimental demonstrations of complementary acoustic metamaterials have been scarce due to the challenges in precisely prototyping either the membrane [23, 26] or intricate metallic meta-atoms [25]. For the limited experimental realizations of complementary acoustic metamaterials [27], though energy transmission improvements were demonstrated for weakly impedance-mismatched layers (e.g., plastic or resin barrier layers in water), the same approach may not be equally effective for through-metal-wall power transfer where relative large impedance mismatch is present. In addition to complementary metamaterials, an inversely optimized auxiliary meta-lens [28] has been demonstrated to assist the focusing enhancement through a 1.8 mm metallic wall in water at 200 kHz. However, the overall power transmission rate was not quantitatively analyzed. The inverse optimization method used for designing the meta-lens also may not be applicable for all general physical scenarios.

In this paper, we present a metamaterial-based approach to enable WC-UPT and WC-UDT through a metallic wall immersed in a strongly impedance-mismatched background medium. A deterministic method based on the band structure theory and transmission analyses is utilized to design an ultrasonic pillar-based metamaterial. The vertical elongation mode

(VEM) of the pillars is harnessed to achieve ultrasonic power transmission enhancement through the metallic wall without direct contact with transducers. This effectively addresses the notorious couplant degradation issue that is a characteristic of conventional methods in W-UPT and W-UDT. We numerically and experimentally demonstrate that the metamaterial, fabricated by the SLS (selective laser sintering) additive manufacturing technology, enables a 33-fold ultrasonic power transmission rate enhancement from 2% to around 66% near 450 kHz through a 1 mm thick SUS316L plate, whose impedance is 29 times of the background medium water. In addition, a commercial red light-emitting diode (LED) is successfully lit up by harvesting the enhanced transmission of ultrasonic energy, which cannot be lit up without the metamaterial even at an input voltage that is close to five times greater. Benefiting from the enhanced signal-to-noise ratio (SNR) of the received signal, WC-UDT is also demonstrated by transmitting an image using amplitude shift keying (ASK) modulation at a small input voltage.

PILLAR-BASED ACOUSTIC METAMATERIAL

Figure 1 illustrates the working principle of the proposed WC-UPT and WC-UDT. A pair of co-axially aligned PZT transducers are placed on opposite sides of a metallic wall immersed in the background medium (e.g., water), working as a transmitter and a receiver, respectively. A pillar-based acoustic metamaterial, which has been studied in the past to reduce sound transmission through a thin and lightweight barrier in noise control [29, 30], is now proposed to conversely enhance the power transfer through the metallic wall. The proposed pillar-based acoustic metamaterial is composed of periodically arranged pillars (with periodicity p) distributed on the metallic wall (with thickness t), as shown in the close-up views in the top-right and bottom-left corners of Figure 1. Each pillar is fundamentally an acoustic spring-mass resonator, in which the large cylinder (with diameter d_m and height h_{m2}) works as a "mass" and the smaller cylinder (with diameter d_s and height h_s) works as a "spring". In this study, the pillar is assumed to be made of the same material as the wall, and is tapered with a height of h_{m1} between two cylinders in order to facilitate 3D printing at a high accuracy. Once the resonant frequency of the pillar-based acoustic metamaterial is carefully tuned towards the working frequency of transducers, the ultrasonic wave generated by the transmitter can propagate through the metallic wall and excite a strong vibration of the pillars. The resonating pillars, as shown by the distribution of the normalized displacement magnitude $|u|$ in the top-right corner of Figure 1, will work as secondary acoustic sources to re-radiate the ultrasonic wave to the other side of the wall, which would otherwise have a very limited power transmission without the metamaterial. Subsequently, the receiver can convert the metamaterial-enhanced ultrasonic signal back to electrical signal to power electronics or simply receive the signal for data transmission.

To demonstrate WC-UPT, we adopt a $t = 1\,\text{mm}$ steel (SUS316L) wall in water and a pair of PZT transducers with a center frequency around 500 kHz. The pillar-based acoustic metamaterial is designed based on the modes observed from the calculated band structure. Figure 2a shows one unit cell of the proposed acoustic metamaterial distributed on the wall. The incident pressure is $p_{\text{in}} = P_{\text{in}} e^{j(-k_x x - k_y y - k_z z)} e^{j\omega t}$, in which $k_x = k\sin\theta\cos\phi$, $k_y = k\sin\theta\sin\phi$, $k_z = k\cos\theta$, and $k = \omega/c_0$. c_0 is the sound velocity in water. θ and ϕ are the polar and azimuthal angles of incidence, respectively. Figure 2b shows the numerical calculation (see Appendix A for details) of the complex band structure for the periodically arranged unit cells along the edges of the first irreducible Brillouin zone $\Gamma^{\smile} X^{\smile} M$ as shown in Figure 2a. The size of the unit cell is $p = 1.5\,\text{mm}$ (half wavelength at 500 kHz), $d_s = 0.54\,\text{mm}$, $d_m = 1.35\,\text{mm}$, $h_s = 0.3\,\text{mm}$, $h_{m1} = 0.405\,\text{mm}$, and $h_{m2} = 0.615\,\text{mm}$. In what follows, we will only focus on the wave dispersion along the $\Gamma^{\smile} X$ direction (i.e., y component of the wave vector is zero), as the same physical behaviors can be observed for the other directions. The imaginary eigenfrequency is resulted from the Plane Wave Radiation boundary condition applied on both incoming and outgoing planes. These modes with a large imaginary eigenfrequency are decaying fast in time (or highly evanescent in space since the speed of sound is real) and cannot transmit wave from one side of wall to the other side. For these modes with a small imaginary eigenfrequency, the distribution of the normalized displacement magnitude $|u|$ at Γ point near 500 kHz is plotted to help understand the induced resonances and anti-resonances from the coupling between the wall (plate) and pillars. Here, the anti-resonances are modes where the vibrational amplitude at the plate becomes zero, suggesting that the transmission through the plate is not allowed, whereas the resonances correspond to a non-zero vibrational amplitude at the plate and thus have the potential to enhance transmission [31]. Near 500 kHz, while (γ_1, γ_2) is one pair of degenerate anti-resonance modes, δ is a vertically elongation resonant mode with a successively stretching and compressing motion of the pillars along the vertical direction z. Based on the law of the momentum conservation, δ can be excited when the incident wave has a normal wave component (i.e., $\theta = 0$ and $\phi = 0$). The flat band frequency at which the δ mode [32] arises can be adjusted by altering the geometric parameters of the tapered pillar. Since the mode shape of δ essentially behaves like a spring-mass system, the mode frequency $f \propto \sqrt{\frac{k}{m}} \propto \sqrt{\frac{(\frac{\pi}{4} d_s^2) E_s / h_s}{\rho_s h_{m2} (\frac{\pi}{4} d_{m2}^2) + \frac{1}{3} \rho_s h_{m1} (\frac{\pi d_m^2}{4} + \frac{\pi d_s^2}{4} + \frac{\pi d_m d_s}{4})}}$. For in-

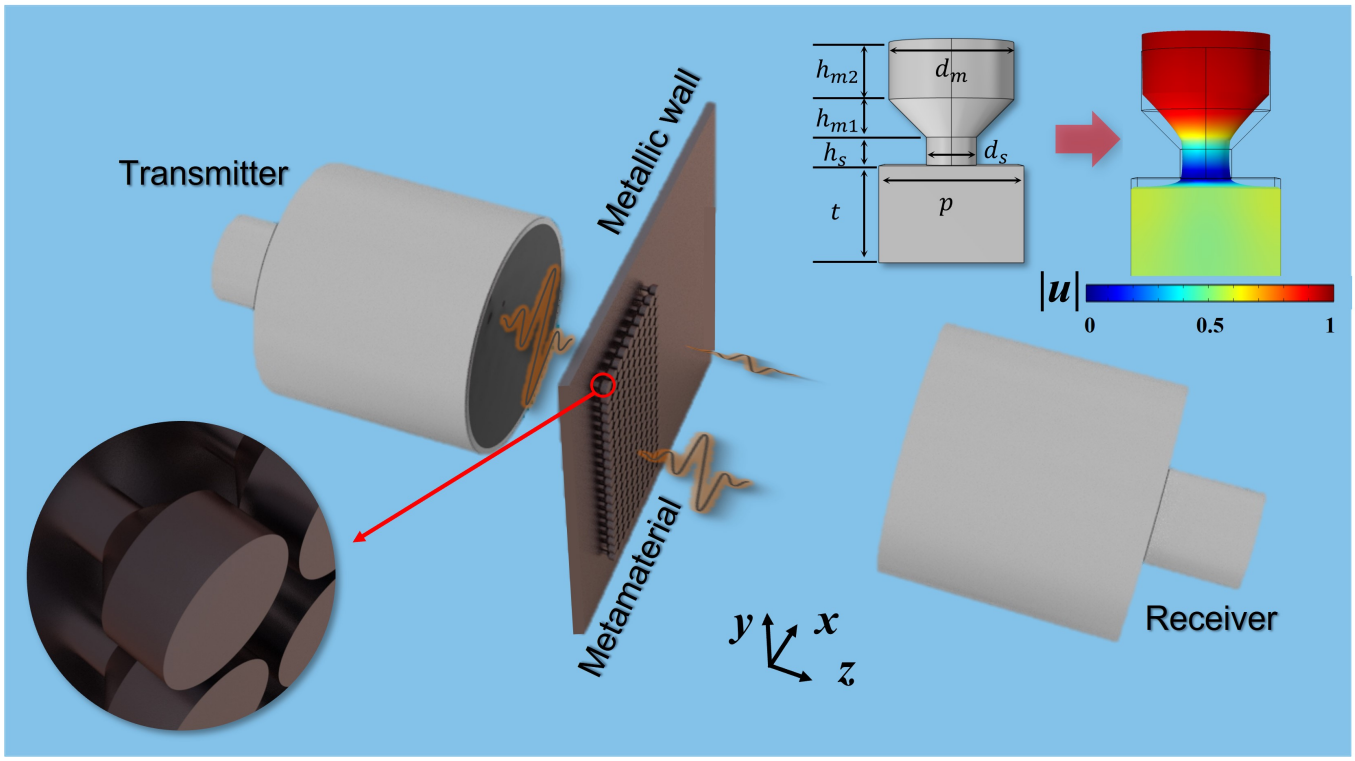

FIG. 1. Schematic of the through-metal-wall WC-UPT and WC-UDT system enabled by the pillar-based acoustic metamaterial. A close-up view of the metamaterial is displayed in the bottom-left corner. The displacement field of the metamaterial at VEM is shown in the top-right corner, which is the mechanism used to enhance the ultrasonic power transmission rate through the metallic wall.

stance, by decreasing the size of the "mass" ($h_{m2}(\frac{\pi}{4}d_{m2}^2)$) or increasing the cross-section ($\frac{\pi}{4}d_s^2$) of the "spring" can increase the vertical elongation mode frequency at which we enhance the transmission through the metallic barrier.

The extent to which the transmission enhancement enabled by the pillar-based acoustic metamaterial can be further assessed by numerical transmission analyses in the frequency range between 300 kHz and 600 kHz. We first study the impact of the number of unit cells on the power transmission rate, which is evaluated under a normally incident plane wave. These results are shown in Figure 2c and illustrate that the power transmission rate increases from 1.9% to 72.3% at 460 kHz when an infinite number of the designed pillar-based acoustic metamaterial units are periodically attached to a 1 mm SUS316L plate. The real eigenfrequency of 459 kHz obtained from the band structure calculation closely aligns with the peak transmission frequency of 460 kHz observed in the transmission analyses. Typical material loss of SUS316L [33] is evaluated and it barely affects the power transmission rate according to our numerical simulations (See Note S1 in the Supplemental Material for details). The surface impedance analysis was used to reveal how the pillars change the effective impedance of the metallic plate as shown in Note S12 of the Supplemental Material. For practical considerations, a series of numerical calculations for different finite numbers of unit cells attached on an infinitely large wall are conducted, and they show that 20×20 unit cells can achieve a power transmission rate of 67.3%, which sufficiently approaches that obtained from an infinite number of unit cells (See Note S2 in the Supplemental Material for detailed simulation setup). This verifies the hypothesis of using the resonance mechanism of VEM to enhance power transmission, which is inferred from the observations in the band structure calculation. In addition, the power transmission rate with respect to the angle of incidence is numerically evaluated, where θ varies from 0° to 60° and $\phi = 0°$. Since there is no wave component on the y direction when $\phi = 0°$, 20 unit cells are simulated along the x direction, and 1 unit cell is simulated along the y direction with a continuity boundary condition to reduce computational costs (See Note S3 in the Supplemental Material for the detailed setup of simulations). The results are shown in Figure 2d and indicate that the power transmission rate can stay at a large magnitude (more than 70%) for a wide range of angles of incidence from 0° to 60°, when excited at the proper frequency. For smaller angles of incidence though, the optimal frequency remains relatively constant and is around 460 kHz.

The generality of the pillar-based acoustic metamaterial on through-metal-wall power transmission enhance-

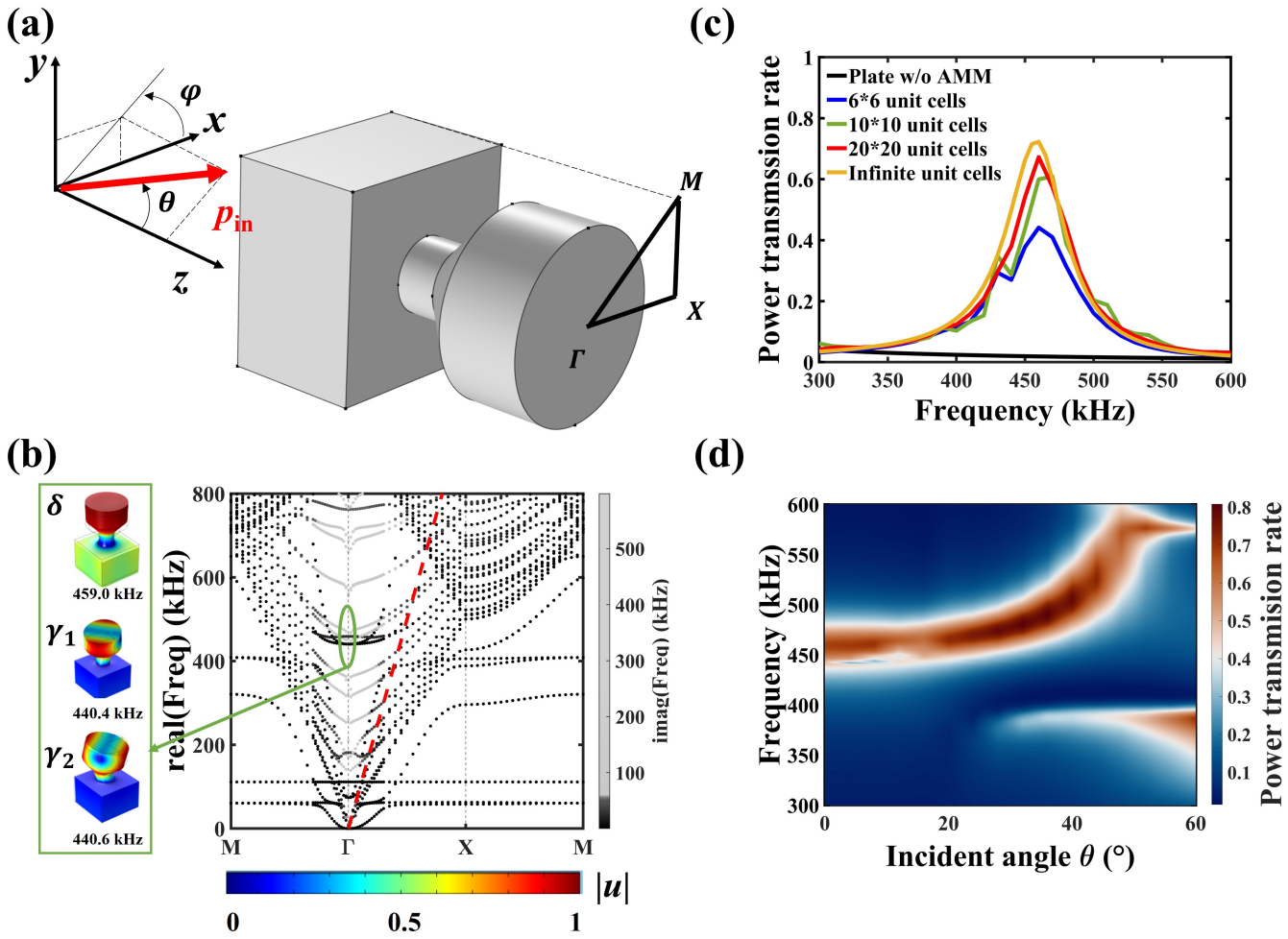

FIG. 2. Design of the pillar-based metamaterial for the through-metal-wall WC-UPT and WC-UDT. a) Schematic of a periodically arranged unit cell under a incident plane wave and the first irreducible Brillouin zone. b) The complex band structure. The real eigenfrequency is plotted on y axis and the imaginary eigenfrequency is represented by the gray scale. The green ellipse encompasses three propagating modes corresponding to δ, γ_1, and γ_2. The distribution of the normalized displacement magnitude |u| for these modes is depicted by the color scale. The red dash line is the sound line. c) Power transmission rate for different number of unit cells under a normally incident plane wave. d) Power transmission rate as a function of the incident angle of θ when $\phi = 0$.

ment is numerically confirmed in the background medium of air, where the impedance contrast is around 104,850. Note S4 in the Supplemental Material shows that the power transmission rate is 0.00001% around 50 kHz through a 1 mm thick SUS316L bare plate immersed in air, and it can be enhanced by at least four orders of magnitude to 20%, 2%, 0.6% or 0.15%, when the loss factor of SUS316L for AMM is set as 0.0001, 0.0005, 0.001 and 0.002, respectively. Unlike the waterborne case, the power transmission rate for the airborne case is inherently ultra-sensitive to the loss factor and has a narrower bandwidth, as shown in Figure S4. These are likely originated from the substantial impedance mismatch between the air and SUS316L, and would place a demand on advanced 3D additive metal printing to precisely control the loss factor for experimental validations.

To further demonstrate the philosophy of using the pillar-based acoustic metamaterial for ultrasonic power transmission enhancement, the waterborne case is experimentally validated against numerical simulations, using the state-of-the-art 3D metal printing technology. A 42 mm × 42 mm × 1 mm wall ($L \times L \times t$, L is the side length) decorated with 20 × 20 aforementioned pillars is under an excitation from a PZT transducer with a diameter $d = 2a = 1$ inch and a central frequency around 500 kHz. Figure 3a and Figure 3b show the schematic and photo of the experimental setup. The origin of the coordinate is set at the center of the transmitter surface and the on-axial propagating direction of the transmitter aligns with the positive z direction. Since the on-axis pressure mag-

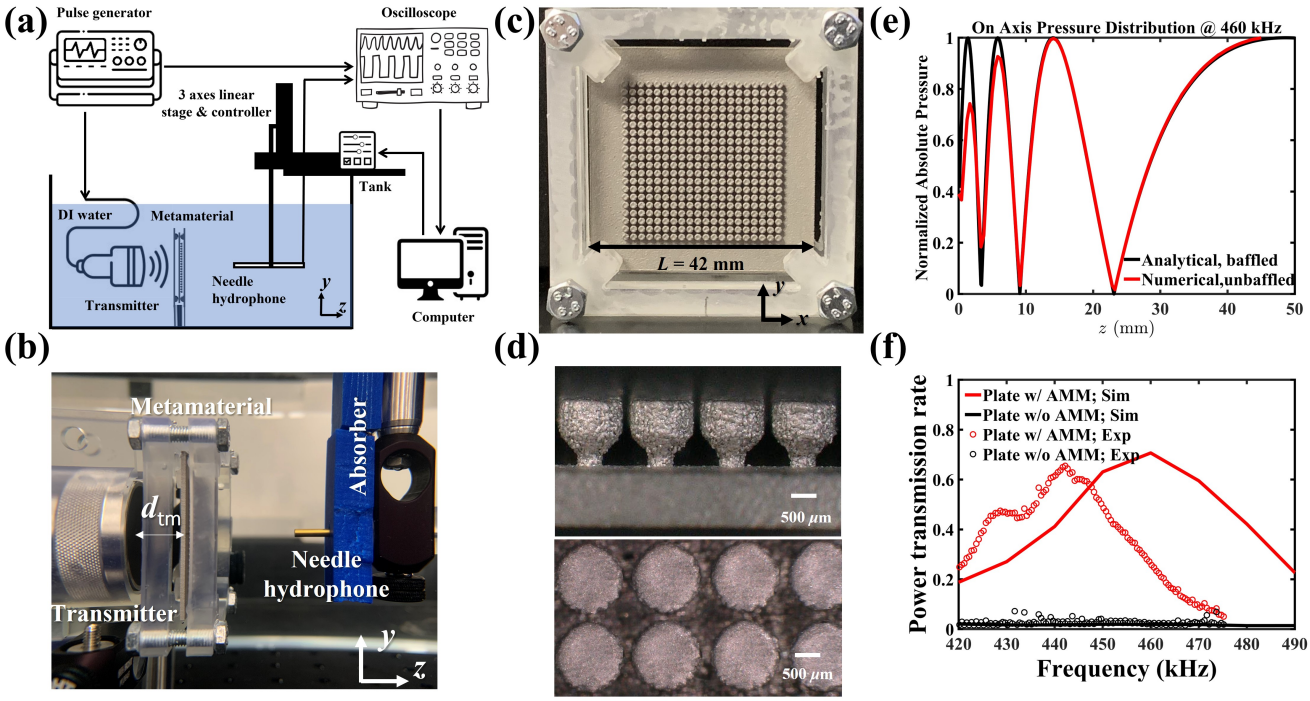

FIG. 3. a) and b) show the schematic and photo of the experimental setup. c) and d) show the fabricated plate with AMMs. e) The on-axis pressure magnitude distribution has multiple local extremes in the near field of the piston transmitter. f) Comparison of simulated and measured power transmission rate.

nitude has multiple local extremes in the near field of the piston transmitter as shown in Figure 3e (Details of simulated radiation field of the transmitter are referenced to Note S6 in the Supplemental Material), the plate with or without AMM is placed at the farthest maximum from the transmitter for the ease of experimental implementations, that is $d_{\rm tm} = a(a/(m\lambda_0) - m\lambda_0/(4{*}a)) = 14$ mm for $m = 3$ (the third extreme moving in toward the transmitter) [34] at $f_0 = 460$ kHz. However, we note that the power transmission rate is insensitive to $d_{\rm tm}$, as supported by the same transmission enhancement achieved when the plate is placed at the minimal pressure location in the near field of the transmitter (Details are referenced to Note S7 in the Supplemental Material). Figure 3c shows the photo of the plate with AMM fabricated by SLS technology (see Appendix B for details), and Figure 3d shows a close-up view. A needle hydrophone scans the transmitted pressure field at the other side of the plate in both x-y plane and x-z plane for three configurations ("No Plate", "Plate w/ AMM", and "Plate w/o AMM"), as shown in Figure 4. Details of experimental measurements are referred to Appendix C and Note S8 in the Supplemental Material. The simulated and measured pressure amplitude distribution in x-y plane is retrieved at $z = 45$ mm, which is close to the Rayleigh distance, as shown in Figure 4a and Figure 4b. The Rayleigh distance, $L_R = d^2/(4\lambda_0)$, is the transition point between the near field and far field, and it is the preferred location for a receiving transducer to tap the maximum power from the transmitter [35]. Pressure amplitude distribution in x-z plane is plotted at $y = 0$ mm in Figure 4c and Figure 4d for numerical and experimental results, respectively. The displayed pressure field is at the peak power transmission frequency, which is 442 kHz for the measurements and 460 kHz for the simulations. Then, the amount of power at the transmitted side is estimated based on the square of pressure amplitude at the surface of $z = 45$ mm, which is a reasonable approximation when transitioning to the far field (See Note S11 in the Supplemental Material for details). The power transmission rate for the "Plate w AMM" and "Plate w/o AMM" configurations can be obtained by normalizing the power transmission of each respective plate configuration to that of the reference "No Plate" configuration. Figure 3f shows a comparison of simulated and measured power transmission rate for the plate with and without AMM. The measured power transmission rate for the 1 mm bare plate is approximately 2% around 442 kHz. In contrast, with the addition of AMM on top of the plate, the measured power transmission is boosted to 65.5% at 442 Hz, with a half-power bandwidth of 33 kHz. Except the slight frequency shift (which is likely due to imperfect fabrication and details are referenced to Note S5 in the Supporting Informatio), a good agreement is observed between measured and simulated results, showing the expected power transmission enhancement enabled by the

AMM.

WIRELESS AND CONTACTLESS ULTRASONIC POWER TRANSFER

With the verified capability of transmission enhancement through the metallic wall, the pillar-based acoustic metamaterial is then employed to realize a WC-UPT. Figure 5a shows the schematic and photo of energy harvesting through the metal wall, with a larger transducer (1.5 inch diameter, 400 kHz resonant frequency) being placed at $z = 45$ mm as a receiver to collect the transmitted ultrasound power to the maximal extent. The receiver is characterized by the impedance spectrum measurement and the optimal power transfer test using a resistive load [36, 37] (See Note S9 in the Supplemental Material for details).

Next, we demonstrate that the enhanced ultrasonic power transmission is harvested to charge a series of capacitors and light up a commercial LED, which is otherwise impossible through a bare plate. Figure 5b shows the measured output signals of the receiver under an excitation of 445 kHz continuous-mode ultrasound for four different configurations: an input voltage of 4.4 Vpp on the transmitter for (i) "No Plate", (ii) "Plate w/ AMM", and (iii) "Plate w/o AMM", as well as (iv) an input voltage of 20 Vpp on the transmitter for "Plate w/o AMM". The alternating current (AC) collected by the receiver is not a feasible power source for most electronics. Therefore, the AC signal is rectified into a DC signal using a pre-designed full-wave-bridge-rectification circuit (See Note S10 in the Supplemental Material for details about the circuit design). Figure 5c shows the measured DC signals stored on a 220 µF during the charging process for more than 400 s until the voltage rise becomes gradual and approaches saturation. While the amplitudes of AC output signals are read as (i) 0.334 V, (ii) 0.264 V, (iii) 0.036 V, and (iv) 0.199 V, the DC voltage on each capacitor is (i) 0.317 V, (ii) 0.220 V, (iii) 0.012 V, and (iv) 0.123 V. The slight voltage drop from AC to DC is mainly caused by the built-in voltage drop across the diodes of the rectifier. Considering the threshold voltage to light up a red LED is around 2 V, 7 series-connected capacitors in the first configuration "No Plate" collect 2.22 V, as shown in Figure 5d, which is enough to light up the LED. The power is also evaluated in the process, which is given by [38] $\bar{P} = C_s V_s^2/(2T)$, where C_s is the capacitance, T is the charging time, and V_s is the stored DC voltage. Thus, the energy stored on the capacitors in the first configuration is increased by $77.4\,\mu$J in 424 s, indicating that the power output capability is 182 nW. In the second case of "Plate w/ AMM", 10 series-connected capacitors reaches 2.1 V with a output power of 116 nW, to successfully light up the LED as shown in Figure 5e. The output power of the second case is calculated as 64% of the first case, in good accordance with the measured power transmission coefficient 65.5% in Figure 3d. However, for the third case of "Plate w/o AMM", the total voltage on 10 series-connected capacitors is only 1.2 V, which is insufficient to power the LED, even when a 20 Vpp excitation was applied to the transmitter (which is the fourth case of "Plate w/o AMM"). Movies that record the charging process and LED illumination are available in Supplemental Material. Details about the energy harvesting circuit is referred to Note S10 in the Supplemental Material.

WIRELESS AND CONTACTLESS ULTRASONIC DATA TRANSMISSION

In addition to WC-UPT, WC-UDT is also demonstrated using the same setup in Figure 5a. Instead of using the continuous mode at a large input voltage for power transfer, burst-mode sinusoidal signals under ASK modulation are fed into the transducer at a small input voltage (25 mV) to transmit the encoded binary data. The received signals, having undergone SNR enhancement facilitated by AMM, can then be amenable to decoding. Using a string of 15-bits data (which is the signal of 15th column in Figures 6(b)-(e)) as an example, Figure 6a showcases the encoding and decoding communication process of WC-UDT: (i) The 15-bits binary signal is first embedded within start bits (100) and stop bits (001). (ii) A time-domain digital signal is generated to transmit the 21-bits binary signal using ASK modulation, and is then fed into the transmitting transducer. Here, each bit is represented by 5 cycles of sine waves at 445 kHz. 21 bits are transmitted every 0.4 ms and the communication speed is 52.5k bps. The digital power, which is defined as the summation of the voltage square for every 5 cycles of sine waves, is proposed as an algorithm to characterize the quality of the transmitted digital signal and extract data from the received digital signal. As shown by the orange curve, the line-shape of the digital power for the transmitted signal agrees perfectly with the binary signal, showing the good quality of the transmitted signal. (iii) Despite a slight distortion in the received digital signal mainly caused by the frequency response of the transducer pair, the decoded signal, obtained by computing its digital power, exhibits a strong correspondence with the transmitted signal in the presence of AMM. (iv) In the absence of AMM, the transmitted signals is weaker and strongly contaminated by the noise. Consequently, the recovery of the transmitted signal from the received signal becomes challenging. Next, a more complicated binary image showing letters of "PSU" is used to demonstrate WC-UDT. Figures 6b depicts the original image composed of 15×36 pixels, which is encoded into binary signals of "0" and "1". Figures 6c, d, and e are images of the digital power (normalized by their respective max-

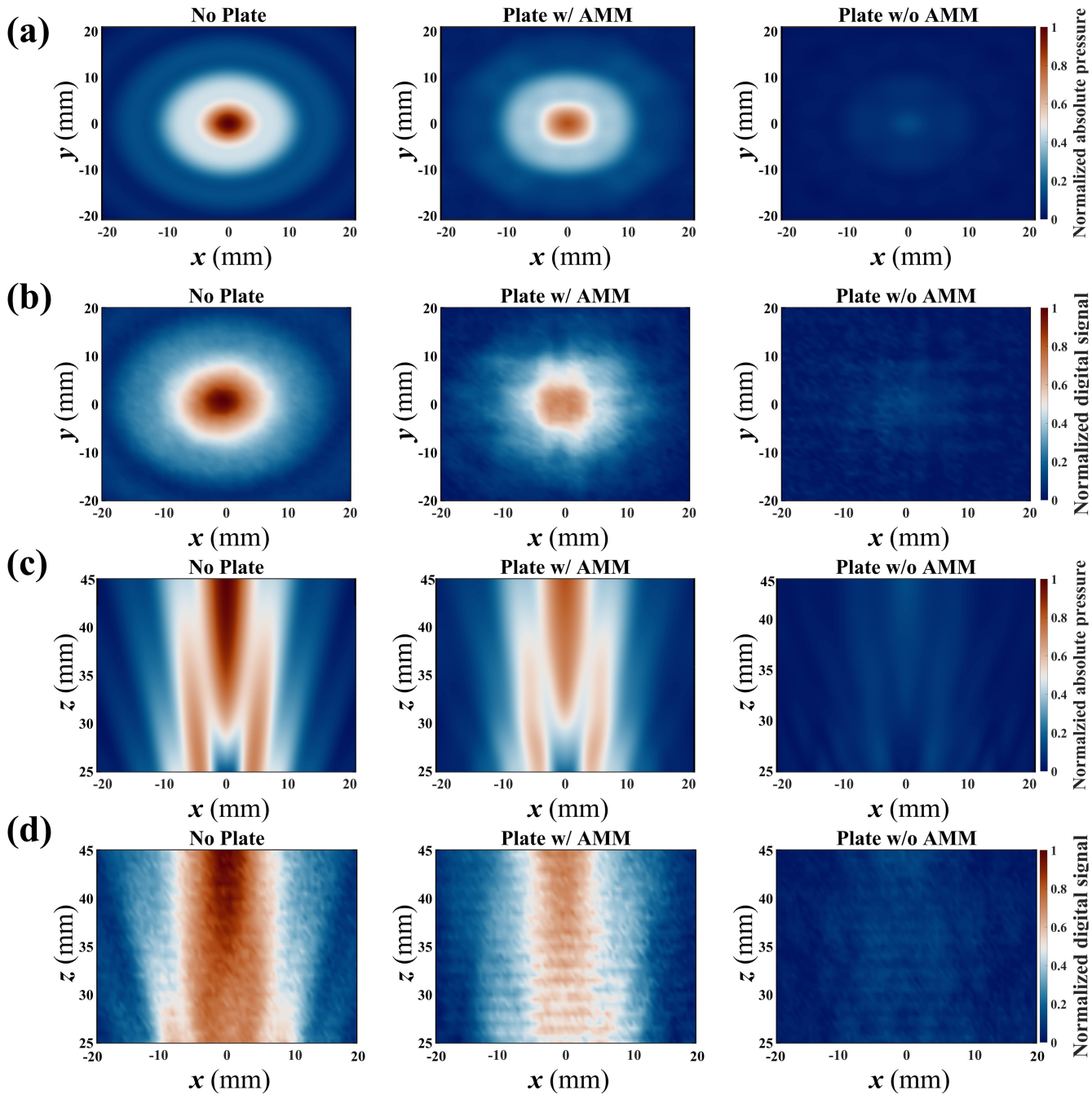

FIG. 4. The transmitted pressure field from numerical simulations (at 460 kHz) and experimental measurements (at 442 kHz) demonstrates the transmission enhancement enabled by AMM. a) Simulated and b) measured pressure field in x-y plane at z = 45 mm. c) Simulated and d) measured pressure field in x-z plane at y = 0 mm. The center of the transmitter surface is set as the origin of the coordinate. For each sub-figure, the pressure magnitude is normalized by the maximum value in the case of "No Plate".

imum digital power) for the transmitted signal, the received signal in the presence of AMM, and the received signal in the absence of AMM, respectively. The implementation of AMM allows for the restoration of a clear image depicting the letters "PSU". In contrast, the absence of AMM yields a noise-dominant recovered image, which necessitates an increase in the input voltage and subsequently incurs a higher power cost.

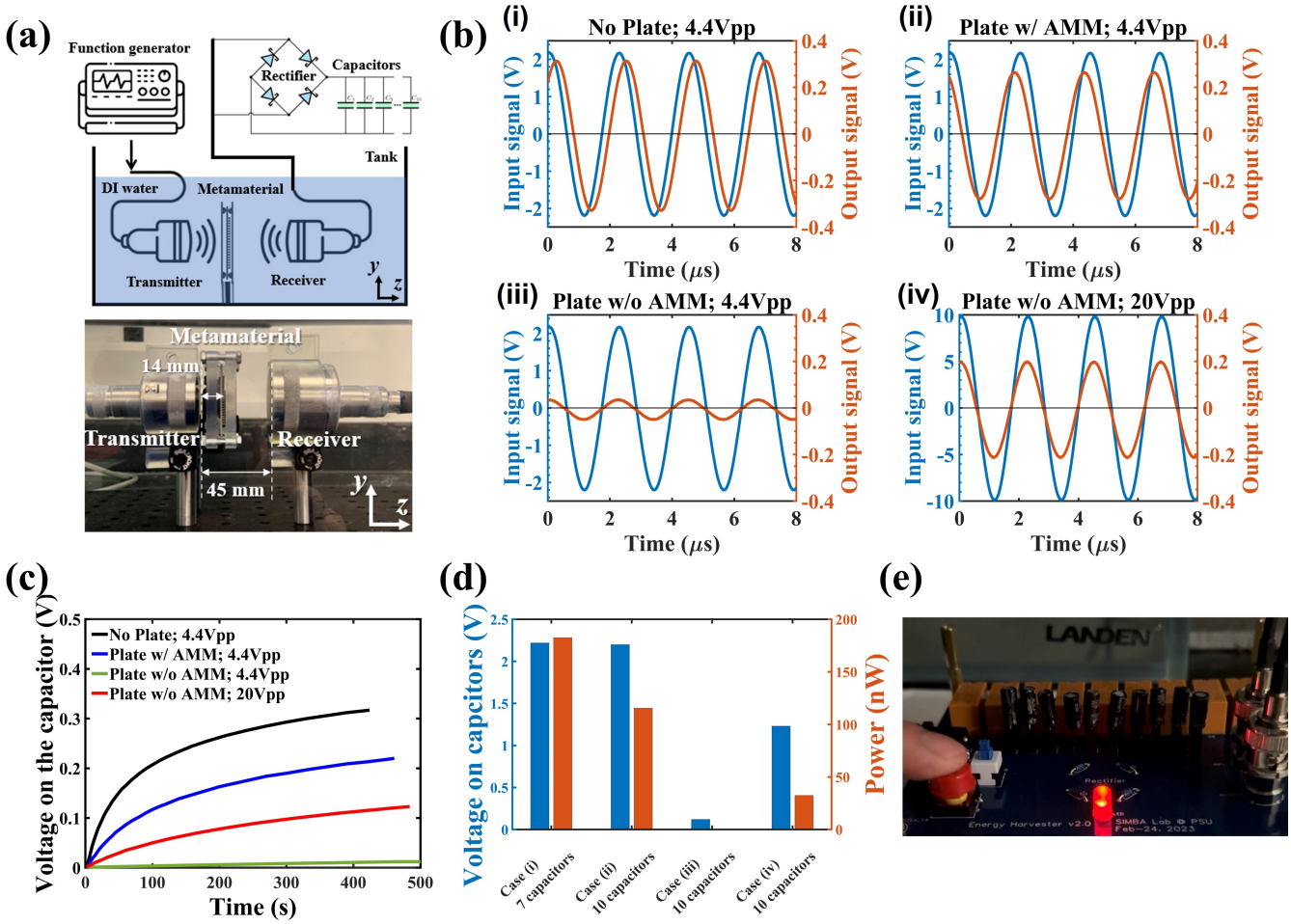

FIG. 5. Experimental results of wireless and contactless ultrasonic power transfer through a metallic wall using the pillar-based metamaterial. a)Schematic and photo of experimental setups. The enhanced ultrasonic transmission is collected by a receiver to charge capacitors. b) The measured output signals of the receiver under an excitation of 445 kHz continuous-mode ultrasound for four different configurations: an input voltage of 4.4 Vpp on the transmitter for (i) "No Plate", (ii) "Plate w/ AMM", and (iii) "Plate w/o AMM", as well as (iv) an input voltage of 20 Vpp on the transmitter for "Plate w/o AMM". c) The charging time dependence of voltage on a 220 μF capacitor for the four configurations. d) Comparison of the charged voltage and average charging power. e) Photo showing that a commercial LED lit up in the configuration (ii).

CONCLUSION

In summary, we have proposed a pillar-based acoustic metamaterial that enables wireless and contactless ultrasound power transfer and data transmission through a metallic plate without any openings. A deterministic method based on band structure theory and transmission analyses is utilized to guide the design procedure. The proposed design is numerically and experimentally verified when the ambient medium is water. Our work not only expands applications for acoustic metamaterial research and 3D metal printing technology, but also sets the direction for the development of next generation of through-metal-wall ultrasonic power transfer and data transmission.

ACKNOWLEDGEMENTS

Y.J. thanks the startup funds from the Pennsylvania State University.

APPENDIX A: NUMERICAL SIMULATIONS

The numerical simulations of were performed using the commercial finite element analysis software COMSOL Multiphysics V6.0. The background medium is water(air) with the density ρ_0 and speed of sound c_0 being 1,000 (1.21) kg/m^3 and 1,500 (343) m/s, respectively. The metallic plate and acoustic metamaterial are SUS316L with the density ρ_s, Young's modulus E_s, and Poisson's ratio ν_s being 7,910 kg/m^3, 153 GPa, and 0.34,

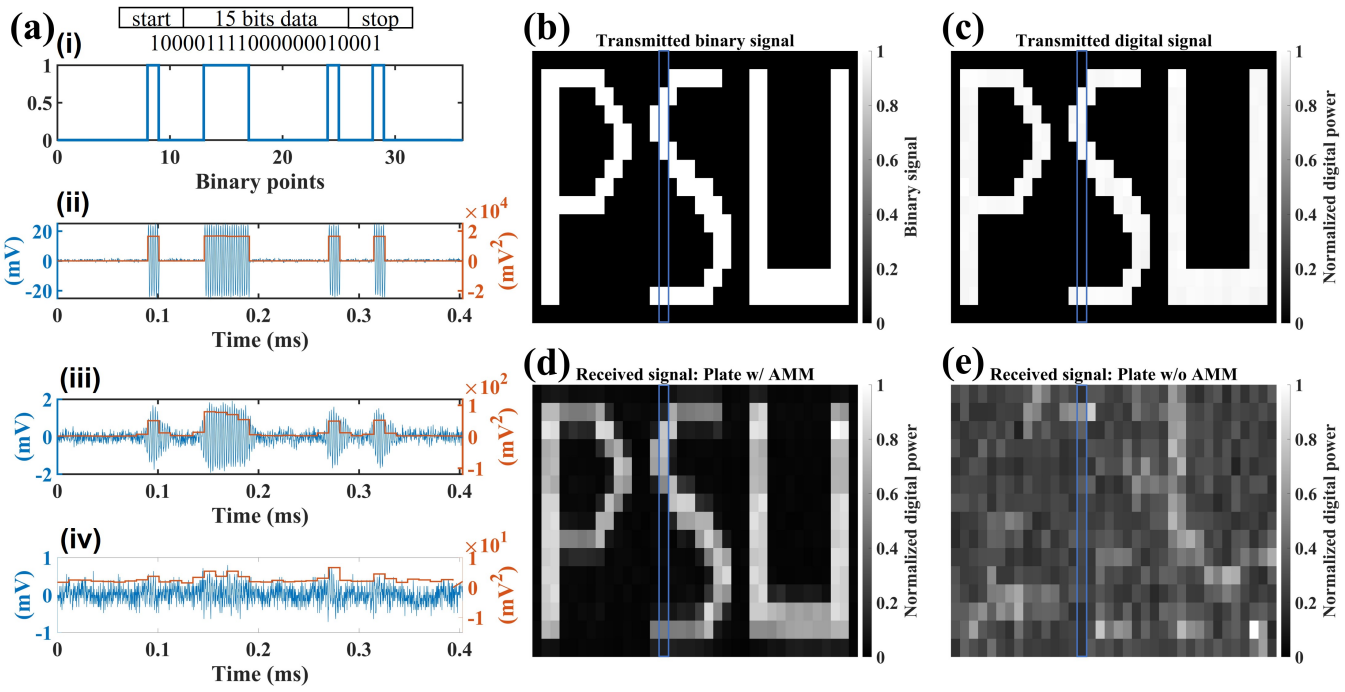

FIG. 6. Experimental results of wireless and contactless ultrasonic data transmission of a binary image of "PSU". a) The transmission of binary data using ASK modulation: (i) a 15-bits binary signal embedded within the start bits (100) and the stop bits (001), (ii) the binary signal is transformed into digital signal before being transmitted through a PZT transducer, in which each bit is represented by 5 cycles of sine waves at 445 kHz, (iii) the received time-domain digital signal for "Plate w/ AMM", and (iv) the received time-domain digital signal for "Plate w/o AMM". For (ii) - (iv), left axis is the digital voltage and right axis is the digital power. b) The original image composed of 15×36 pixels is encoded into binary signals of "0" and "1". c) The transmitted digital image. d) The received digital image for "Plate w/ AMM". e) The received digital image for "Plate w/o AMM". The digital power in (c)-(e) is normalized by their respective maximum digital power. The signals in the 15th column (highlighted by blue blocks) of images in (b)-(e) are shown in (a).

respectively. The equivalent longitudinal speed of sound of SUS316L is $c_l = \sqrt{\frac{K_s+4G_s/3}{\rho_s}} = 5,456\text{m/s}$, where bulk modulus $K_s = E_s/(3(1-2\nu_s))$ and shear modulus $G_s = 0.5E_s/(1+\nu_s)$. The band structure was performed using Solid Mechanics and Pressure Acoustics module where the background medium of water is considered. Plane wave radiation boundary condition is applied at both incoming and outgoing planes so that a complex-valued band structure is obtained. Transmission analysis was performed using Pressure Acoustics and Solid Mechanics modules. More details are referred to Supplemental Material.

APPENDIX B: SAMPLE FABRICATIONS

The sample was fabricated using a commercial 3D printer (Metal 3D Printer ProX™ DMP300) and was based on Selective Laser Sintering (SLS) technology. The printing material is SUS316L, with a nominal resolution of 0.15 mm.

APPENDIX C: EXPERIMENTAL MEASUREMENTS

In the experiment, a 15 in × 23 in × 14 in water tank was used. It was equipped with LC series 3 axes linear stages and a 3 axes stepper motor controller (Newmark Systems, Inc.), travel range 400 mm × 400 mm × 400 mm. The stages were automatically controlled through the programmed code to scan the space. The tank was filled with approximately 7 gallons of deionized water (DI water) and degassed using a water pump and vacuum pump to remove any air bubbles. Unfocused transducers (with a diameter of 1 in and 1.5 in) centered at approximately 500 kHz (Olympus) were used as a transmitter and a receiver. To map the acoustic power distribution, a needle hydrophone (Onda Corps. HNR 0500) with a diameter of 2.5 mm and frequency range of 0.25-10 MHz was used. The transmitter was connected to the arbitrary waveform generator (Agilent 33250A). The receiver and hydrophone were connected to the oscilloscope (Tektronics MDO 3024 Mixed Domain Oscilloscope) to acquire and process the signals. To minimize unwanted reflections and echoes, an ane-

choic absorbing layer of Aptflex F28 from Acoustic Polymers Ltd was attached to the back wall and the post where the hydrophone mounted to. Aptflex F28 is a pre-cast polyurethane sheet that is micro-bubble filled, with density and wave speed similar to that of water. It exhibits high transmission loss ($>$ 30dB/cm/MHz) and High echo-reduction ($>$ 42dB at 1 MHz). The alignment between a source, sample, and receiver was achieved by a laser alignment.

For WC-UPT shown in the video, the transmitter was connected to the function generator Agilent 33250A, and the AC signals on the transmitter and receiver were measured by the oscilloscope. The multi-meter was used to monitor the DC voltage on the capacitors. The actual voltage applied to the transmitter is twice of the value indicated on the screen of the function generator. This is because the function generator assumes a loading impedance of $50\,\Omega$, whereas the impedance of the transmitter far surpasses the internal impedance of the function generator ($50\,\Omega$). All capacitors were connected in parallel and charged when the "SW_CHARGE" switch button was pressed down, while the "SW_WIRING" switch button was not pressed. Once the capacitors were fully charged, the "SW_CHARGE" switch was released to stop the charging process. By pressing down the "SW_WIRING" switch, all capacitors were wired in series. Finally, the "SW_LED" switch button was pressed down to power the LED. More details about the buttons on the circuit board are referred to Note S10 in the Supplemental Material.

For WC-UDT, the discrete time-domain signal with ASK modulation was first generated in MATLAB and then imported into the arbitrary waveform generator (AWG) interface of PicoScope 5442D in order to be fed into the transmitting transducer. The AC signals on the transmitter and receiver were measured by the same oscilloscope.

* J.J., H.H., and J.Z equally contributed to this work.
† mxo5236@psu.edu
‡ yqj5201@psu.edu

[1] D.-X. Yang, Z. Hu, H. Zhao, H.-F. Hu, Y.-Z. Sun, and B.-J. Hou, Through-metal-wall power delivery and data transmission for enclosed sensors: A review, Sensors **15**, 31581 (2015).

[2] M. R. Awal, M. Jusoh, T. Sabapathy, M. R. Kamarudin, and R. A. Rahim, State-of-the-art developments of acoustic energy transfer, International Journal of Antennas and Propagation **2016** (2016).

[3] M. G. Roes, J. L. Duarte, M. A. Hendrix, and E. A. Lomonova, Acoustic energy transfer: A review, IEEE Transactions on Industrial Electronics **60**, 242 (2012).

[4] S. Sherrit, M. Badescu, X. Bao, Y. Bar-Cohen, and Z. Chang, Efficient electromechanical network model for wireless acoustic-electric feed-throughs, in *Smart Structures and Materials 2005: Smart Sensor Technology and Measurement Systems*, Vol. 5758 (SPIE, 2005) pp. 362–372.

[5] S. Sherrit, B. Doty, M. Badescu, X. Bao, Y. Bar-Cohen, J. Aldrich, and Z. Chang, Studies of acoustic-electric feed-throughs for power transmission through structures, in *Smart Structures and Materials 2006: Industrial and Commercial Applications of Smart Structures Technologies*, Vol. 6171 (SPIE, 2006) pp. 8–15.

[6] H. Fu, J. Rao, M. S. Harb, and S. Theodossiades, Ultrasonic wireless power links for battery-free condition monitoring in metallic enclosures, Ultrasonics **114**, 106395 (2021).

[7] K. Sun, Y. Wu, F. Qian, H. Jung, S. Kaluvan, H. Huijin, C. Zhang, F. K. Reed, M. N. Ericson, H. Zhang, *et al.*, Self-powered through-wall communication for dry cask storage monitoring, Annals of Nuclear Energy **177**, 109306 (2022).

[8] S. A. Cummer, J. Christensen, and A. Alù, Controlling sound with acoustic metamaterials, Nature Reviews Materials **1**, 1 (2016).

[9] S. A. Cummer and D. Schurig, One path to acoustic cloaking, New journal of physics **9**, 45 (2007).

[10] H. Chen and C. T. Chan, Acoustic cloaking in three dimensions using acoustic metamaterials, Applied physics letters **91**, 183518 (2007).

[11] A. N. Norris, Acoustic cloaking theory, Proceedings of the Royal Society A: Mathematical, Physical and Engineering Sciences **464**, 2411 (2008).

[12] J. Li, L. Fok, X. Yin, G. Bartal, and X. Zhang, Experimental demonstration of an acoustic magnifying hyperlens, Nature materials **8**, 931 (2009).

[13] J. Zhu, J. Christensen, J. Jung, L. Martin-Moreno, X. Yin, L. Fok, X. Zhang, and F. Garcia-Vidal, A holey-structured metamaterial for acoustic deep-subwavelength imaging, Nature physics **7**, 52 (2011).

[14] N. Kaina, F. Lemoult, M. Fink, and G. Lerosey, Negative refractive index and acoustic superlens from multiple scattering in single negative metamaterials, Nature **525**, 77 (2015).

[15] X. Zhu, H. Ramezani, C. Shi, J. Zhu, and X. Zhang, P t-symmetric acoustics, Physical Review X **4**, 031042 (2014).

[16] C. Shi, M. Dubois, Y. Chen, L. Cheng, H. Ramezani, Y. Wang, and X. Zhang, Accessing the exceptional points of parity-time symmetric acoustics, Nature communications **7**, 11110 (2016).

[17] R. Fleury and A. Alù, Extraordinary sound transmission through density-near-zero ultranarrow channels, Physical review letters **111**, 055501 (2013).

[18] J. J. Park, K. Lee, O. B. Wright, M. K. Jung, and S. H. Lee, Giant acoustic concentration by extraordinary transmission in zero-mass metamaterials, Physical review letters **110**, 244302 (2013).

[19] Y. Zhou, M.-H. Lu, L. Feng, X. Ni, Y.-F. Chen, Y.-Y. Zhu, S.-N. Zhu, and N.-B. Ming, Acoustic surface evanescent wave and its dominant contribution to extraordinary acoustic transmission and collimation of sound, Physical review letters **104**, 164301 (2010).

[20] H. Estrada, P. Candelas, A. Uris, F. Belmar, F. G. De Abajo, and F. Meseguer, Extraordinary sound screening in perforated plates, Physical review letters **101**, 084302 (2008).

[21] J. Christensen, L. Martin-Moreno, and F. J. Garcia-

Vidal, Theory of resonant acoustic transmission through subwavelength apertures, Physical review letters **101**, 014301 (2008).

[22] M.-H. Lu, X.-K. Liu, L. Feng, J. Li, C.-P. Huang, Y.-F. Chen, Y.-Y. Zhu, S.-N. Zhu, and N.-B. Ming, Extraordinary acoustic transmission through a 1d grating with very narrow apertures, Physical review letters **99**, 174301 (2007).

[23] C. Shen, J. Xu, N. X. Fang, and Y. Jing, Anisotropic complementary acoustic metamaterial for canceling out aberrating layers, Physical Review X **4**, 041033 (2014).

[24] S. R. Craig, P. J. Welch, and C. Shi, Non-hermitian complementary acoustic metamaterials for lossy barriers, Applied Physics Letters **115**, 051903 (2019).

[25] C. I. Park, C. Piao, H. Lee, and Y. Y. Kim, Elastic complementary meta-layer for ultrasound penetration through solid/liquid/gas barriers, International Journal of Mechanical Sciences **206**, 106619 (2021).

[26] J. Wang, F. Allein, N. Boechler, J. Friend, and O. Vazquez-Mena, Design and fabrication of negative-refractive-index metamaterial unit cells for near-megahertz enhanced acoustic transmission in biomedical ultrasound applications, Physical Review Applied **15**, 024025 (2021).

[27] L. Li, Y. Diao, H. Wu, and W. Jiang, Complementary acoustic metamaterial for penetrating aberration layers, ACS Applied Materials & Interfaces **14**, 28604 (2022).

[28] H. Gao, Z. Gu, S. Liang, T. Liu, J. Zhu, and Z. Su, Enhancing ultrasound transmission and focusing through a stiff plate with inversely optimized auxiliary meta-lens, Applied Physics Letters **120**, 111701 (2022).

[29] B. Assouar, M. Oudich, and X. Zhou, Acoustic metamaterials for sound mitigation, Comptes Rendus Physique **17**, 524 (2016).

[30] M. Oudich, X. Zhou, and M. Badreddine Assouar, General analytical approach for sound transmission loss analysis through a thick metamaterial plate, Journal of Applied Physics **116**, 193509 (2014).

[31] M. Oudich, B. Djafari-Rouhani, Y. Pennec, M. B. Assouar, and B. Bonello, Negative effective mass density of acoustic metamaterial plate decorated with low frequency resonant pillars, Journal of Applied Physics **116**, 184504 (2014).

[32] M. Oudich, Y. Li, B. M. Assouar, and Z. Hou, A sonic band gap based on the locally resonant phononic plates with stubs, New Journal of Physics **12**, 083049 (2010).

[33] M. F. Ashby, Overview no. 80: On the engineering properties of materials, Acta metallurgica **37**, 1273 (1989).

[34] L. E. Kinsler, A. R. Frey, A. B. Coppens, and J. V. Sanders, *Fundamentals of acoustics* (John wiley & sons, 2000).

[35] K. Agarwal, R. Jegadeesan, Y.-X. Guo, and N. V. Thakor, Wireless power transfer strategies for implantable bioelectronics, IEEE reviews in biomedical engineering **10**, 136 (2017).

[36] S. Qi, M. Oudich, Y. Li, and B. Assouar, Acoustic energy harvesting based on a planar acoustic metamaterial, Applied Physics Letters **108**, 263501 (2016).

[37] M. Oudich and Y. Li, Tunable sub-wavelength acoustic energy harvesting with a metamaterial plate, Journal of Physics D: Applied Physics **50**, 315104 (2017).

[38] L. Jiang, Y. Yang, R. Chen, G. Lu, R. Li, J. Xing, K. K. Shung, M. S. Humayun, J. Zhu, Y. Chen, *et al.*, Ultrasound-induced wireless energy harvesting for potential retinal electrical stimulation application, Advanced Functional Materials **29**, 1902522 (2019).

Supplemental Material for "Metamaterial-enabled wireless and contactless ultrasonic power transfer and data transmission through a metallic wall"

Jun Ji[1,*], Hyeonu Heo[1,*], Jiaxin Zhong[1,*], Mourad Oudich[1,2,†], and Yun Jing[1,‡]

[1]Graduate Program in Acoustics, The Pennsylvania State University, University Park, Pennsylvania, 16802, USA

[2]Université de Lorraine, CNRS, Institut Jean Lamour, F-54000 Nancy, France

December 15, 2023

Contents

*

†

‡

1 The impact of loss factor of SUS316L on the power transmission rate in simulations

To evaluate how loss factor of SUS316L affects the power transmission rate in COMSOL, four different typical values are considered: $\eta = 0.0001$, $\eta = 0.0005$, $\eta = 0.001$, and $\eta = 0.002$. In the simulations, one unit cell is considered under a normally incident wave, and "Continuity" under "Periodic Condition" is applied to both water and SUS316L since there is no wave components along the x and y direction. The loss factor is applied under "Damping" of "Linear Elastic Material". The simulated results in Figure S1 indicate that the typical loss factor of SUS316L barely affects the power transmission rate.

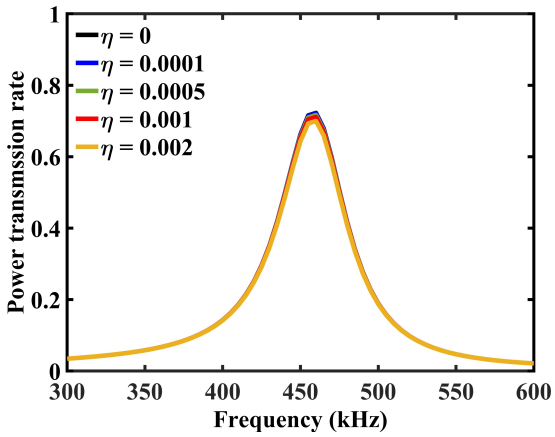

Figure S1: The power transmission rate as a function of SUS316L loss factor in COMSOL.

2 The impact of the number of unit cells on the power transmission rate in simulations

To evaluate how the number of unit cells affects the power transmission rate in COMSOL, three different cases are considered: 6×6, 10×10, and 20×20 unit cells. The size of pillar units in Fig. 2c is maintained the same so that the frequency of the vertical elongation mode and the frequency of the peak power transmission are the same for the scenarios of different number of unit cells. The comparison here is to evaluate how the number of pillar units affects the power transmission if attached on a infinitely large metallic plate. The incident wave is a plane wave normal to the plate surface using "Plane Wave Radiation", and the plate is infinitely large to ignore the backward propagation from the edges by setting "Perfectly Matched Layer" around the plate. The incident and transmitted wave are confined in a waveguide having the same cross sectional area with the metamaterial units to ignore the wave diffraction effect. Only 3×3, 5×5, and 10×10 unit cells are modeled in COMSOL with "Symmetry" boundary condition to reduce computational costs. "Perfectly Matched Layer" is set at the transmission end to reduce the back reflection. The non-perfect plane wave from the transducer effect, the finite plate size effect and the wave diffraction effect are considered in the large sample test in Figure S6. Figure S2 shows the pressure distribution for the three cases at the power transmission peak frequency 460 kHz.

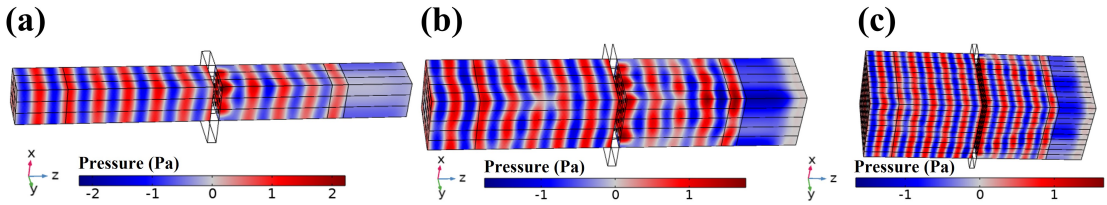

Figure S2: The pressure distribution at the power transmission peak frequency 460 kHz for a) 6×6, b) 10×10, and c) 20×20 unit cells. The middle part without the pressure distribution is the plate region simulated with "Solid Mechanics" module.

3 The impact of the incident angle on the power transmission rate in simulations

To evaluate how the anlge of incidence θ affects the power transmission rate in COMSOL, we have chosen the case of 20×20 units for illustration. Since we have assumed $\phi = 0$, there is no wave component along the y direction. Therefore, we have constructed only one unit cell along the y direction, with "Continuity" under "Periodic Condition" being applied to both water and SUS316L along the y direction to reduce computational costs. The incident wave is applied using "Background Pressure Field" with a parametric sweep of θ from 0° to 60° and the scattered field can be solved from 300 kHz to 600 kHz. "Perfectly Matched Layer" is applied at both the incident and transmitted sides to minimize reflections. The transmitted power is calculated by integrating the default function "Acoustic Intensity" along a surface enclosing the metamaterial at the transmitted side. Figure S3a and Figure S3b illustrate the distribution of the background pressure and the scattered pressure, respectively, when the excitation frequency is 460 kHz and $\theta = 60°$. And a strong transmission can be observed.

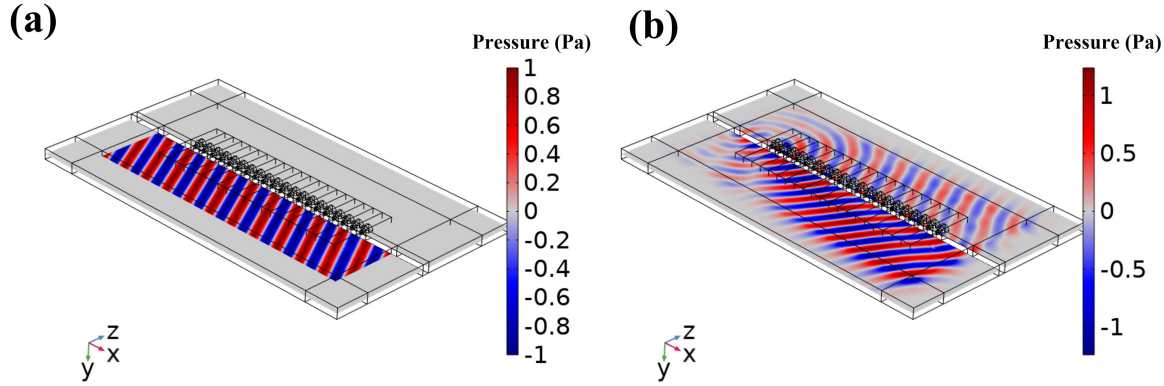

Figure S3: The distribution of a) the background pressure and b) the scattered pressure when the excitation frequency is 460 kHz and $\theta = 60°$.

4 Power transmission enhancement through $t = 1\,\mathrm{mm}$ SUS316L wall in air around 50 kHz

To demonstrate the generality of the design philosophy of power transmission enhancement, a double-sided pillar-based acoustic metamaterial is proposed to enhance ultrasonic power transmission through 1 mm thick SUS316L plate in air, with a 50 kHz ultrasound as the incident wave, as shown in Figure S4a. Considering the huge impedance mismatch between air and SUS316L, identical pillars are distributed

on both sides of the plate to induce a larger vibration for power transmission enhancement. The same procedure with band structure and transmission analyses is utilized to design the metamaterial. The only difference from the water scenario is that the background medium of air is not considered in the band structure calculation since the mass loading effect from air is very small. Consequently, the obtained band structure is purely real. The size of the unit cell is $p = 5.72\,\text{mm}$ (less than one wavelength at 50 kHz), $t = 1\,\text{mm}$, $d_s = 0.42\,\text{mm}$, $d_m = 5.43\,\text{mm}$, $h_s = 0.86\,\text{mm}$, $h_{m1} = 1.15\,\text{mm}$, and $h_{m2} = 6.14\,\text{mm}$. Figure S4b and Figure S4c show the band structure and the power transmission for a unit cell with Floquet periodic condition, respectively. The vertical elongation mode at 50.92 kHz shown in the inset contributes to the power transmission rate enhancement from 0.00001% to near 100% around 51 kHz. Unlike the water-SUS316L case, the air-SUS316L case is ultra-sensitive to the loss factor of SUS316L, as shown in Figure S4d. As the loss factor increases, the peak power transmission rate near 51 kHz is decreased by several orders of magnitude, which is 94%, 20%, 2%, 0.6%, and 0.15% when the loss factor is 0, 0.0001, 0.0005, 0.001, and 0.002, respectively. However, the power transmission rate for the loss factor of 0.002 is still 4 orders of magnitude higher than that without AMM. The nature of being ultra-sensitive to the loss factor and the narrow bandwidth are likely caused by the huge impedance mismatch between the air and SUS316L, which requires more advanced 3D additive metal printing in the future for experimental validations.

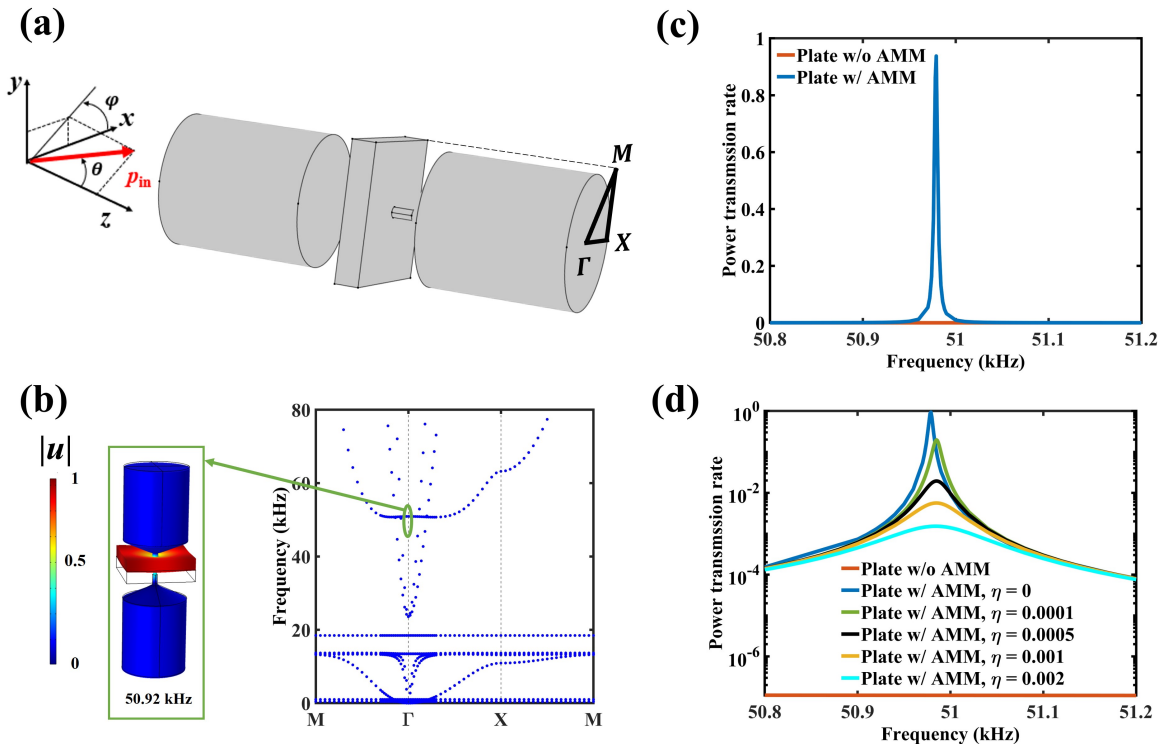

Figure S4: Design of the double-sided pillar-based metamaterial for the power transmission enhancement through a 1 mm metal plate in air at 50 kHz. a) Schematic of a periodically arranged unit cell under a incident plane wave and the first irreducible Brillouin zone. b) Band structure. c) Power transmission rate for the plate w/ and w/O AMM under a normally incident plane wave. d) The typical loss factor of SUS316L significantly affects the power transmission rate.

5 The impact of the fabrication errors on the resonance frequency and power transmission rate in simulations

The impact of fabrication errors on the resonance frequency of a pillar is illustrated in Figure S5. The upper section of the figure shows symmetric (Fig.S5a) and asymmetric (Fig.S5b) pillar shapes, highlighting the influence of asymmetry on the resonance frequency and maximum power transmission rate (Fig.S5c). The lower section of the figure presents an isometric view (Fig.S5d) and a cross-sectional view (Fig.S5e) of a non-flat profile cone-shaped pillar. 3D bar graphs depict the variation of the resonance frequency (Fig.S5f) and the maximum power transmission rate at resonance frequencies (Fig.S5g) with geometric tolerance parameters such as the height (h) and width (w) of the cone shape. The degree of asymmetry does not affect the resonance frequency as long as the mass cylinder is shifted within 2.5% of the mass diameter. Furthermore, the maximum power transmission rate remains unaffected, with changes of less than 0.02%. Although there is relatively noticeable deviation in resonance frequency and power transmission rate due to geometric tolerance, the variations are still acceptable. The non-flat profile cone-shaped pillar exhibits less than 2% and 3% variations in resonance frequency and power transmission rate, respectively, underscoring its robustness.

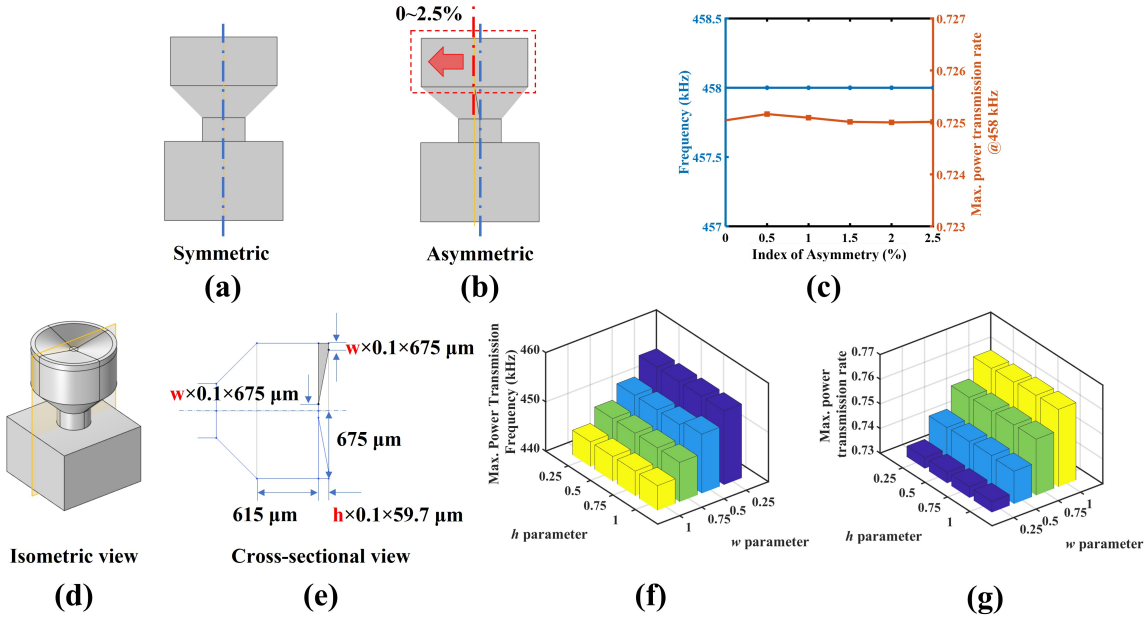

Figure S5: Impact of fabrication errors on the resonance frequency of a pillar and its power transmission rate. (Top) (a) Symmetric and (b) asymmetric shapes. (c) Resonance frequency and power transmission rate (at 458 kHz) affected by degree of asymmetry. (Bottom) (d) Isometric and (e) cross-sectional views. (f) Resonance frequency and power transmission rate bars at resonance frequencies dependent on tolerance parameters, h and w, of the cone shape, respectively.

6 Characteristics of the transmitter

The on-axial pressure field of the unbaffled 1 inch transducer is simulated in COMSOL, and it is compared with the analytical prediction [1] for a baffled piston source at 460 kHz as shown in Figure 3e. The transducer is modeled by imposing "Incident Pressure Field" under "Plane Wave Radiation" on a circle with a diameter of 1 inch. The locations of the multiple local extremes in the near field are matched with the predictions, while the magnitude of the normalized pressure is slightly different from the predictions,

which is mainly cause by the unbaffled condition.

7 The impact of the transmitter-sample distance on the power transmission rate in simulations

A series of large sample simulations are conducted to model the real experimental scenarios. Only 10×10 unit cells are modeled in COMSOL with "Symmetry" boundary condition to reduce computational costs, and a workstation with 1 TB memory is used to run the simulations. The non-perfect plane wave from the transducer effect, the finite plate size effect and the wave diffraction effect are considered in the following ways: 1) The transducer is modeled by imposing "Incident Pressure Field" under "Plane Wave Radiation" on a quarter of the circle with a diameter of 1 inch. 2) "Fixed Constraint" under "Solid Mechanics" is imposed on the corner of the plate to modal the sample holder in experiments. 3) "Perfectly Matched Layer" is set at the surroundings to reduce the back reflection like the anechoic absorbing layer in experiments.

To evaluate how the transmitter-sample distance d_{tm} affects the power transmission rate in COMSOL, two extreme cases in Figure 3e are considered: $d_{\mathrm{tm}} = 14$ mm in which the plate is placed at the far-est maximum on-axial pressure point, and $d_{\mathrm{tm}} = 9.1$ mm in which the plate is placed at the minimal on-axial pressure point. Figure S6a shows that the power transmission rate is almost the same for both cases. At the peak power transmission frequency of 460 kHz, a strong transmission can be attained with AMM, as depicted in the pressure distribution for both cases in Figure S6b.

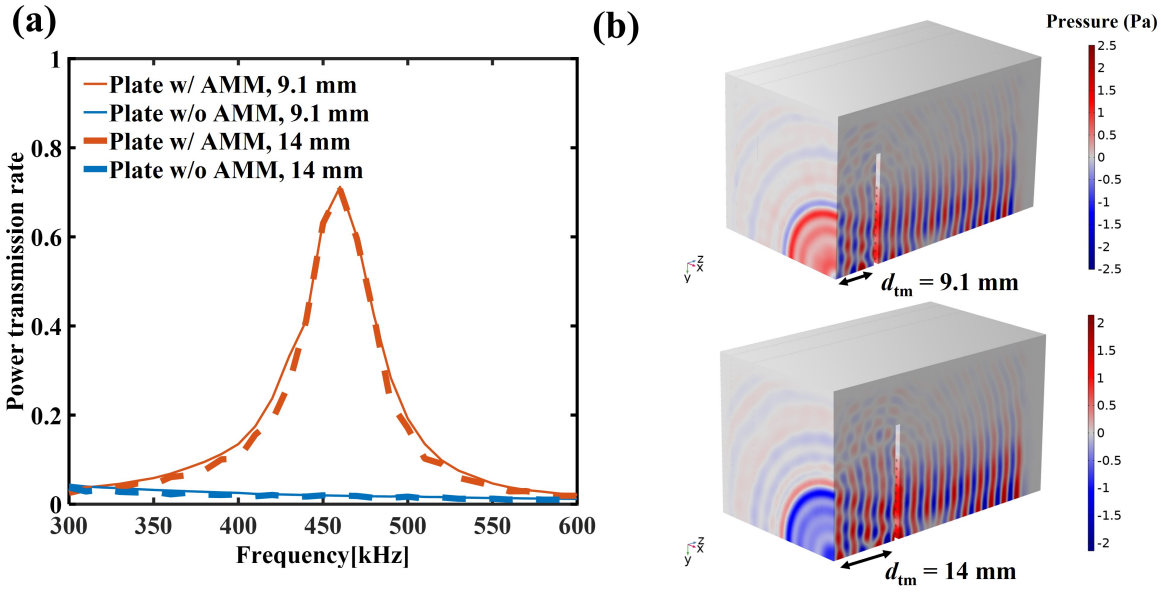

Figure S6: a) The power transmission rate when the plate is placed at the minimal/maximal pressure location in the near field of the transmitter ($d_{\mathrm{tm}} = 9.1$ mm/ 14 mm). b) The pressure distribution for "Plate w/ AMM" at 460 kHz .

8 The measurement of transmitted pressure field

Figure S7 illustrates the emitted and received signals by the transducer and hydrophone, respectively, in both the time and frequency domains for various cases. The emitting signal comprises five cycles in each

burst, with a frequency of 445 kHz, and the burst period is 1 ms. Here, the signal received at a spatial point located at $(x, y, z) = (0, 0, 45\,\text{mm})$ is presented as an example.

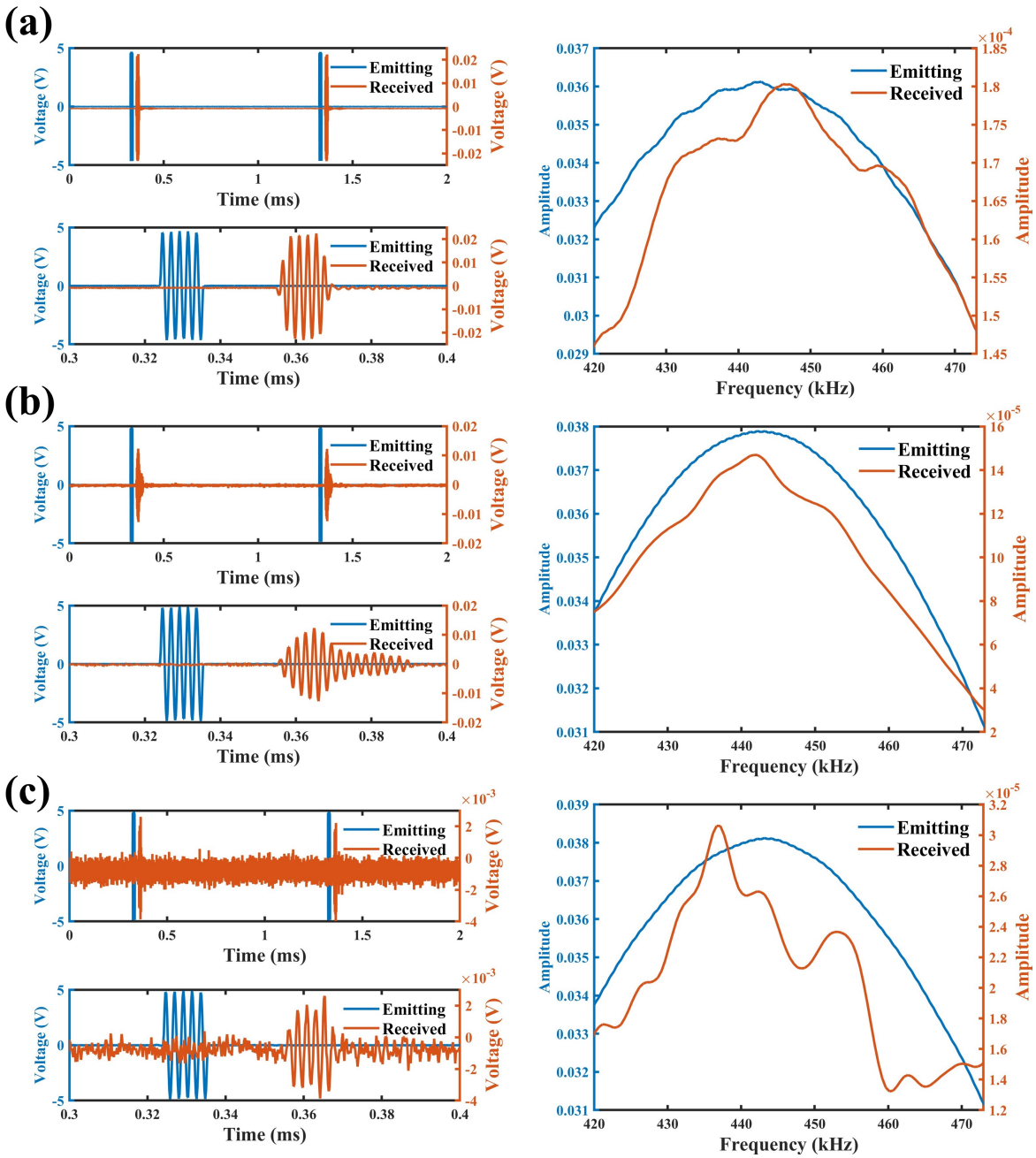

Figure S7: The measured emitting and received signals in the time domain (left column) and frequency domain (right column) for three cases: a) "No plate", b) "Plate w/ AMM", and c) "Plate w/o AMM". For time signals, the top panel displays two periods of the burst and the bottom panel displays the zoomed-in signals.

9 Characteristics of the receiver

Figure S8a shows the measured impedance of the 1.5 inch receiver with a resonant frequency around 400 kHz. The magnitude of the measured impedance is 300 Ω at 460 kHz. Next, the optimal power transfer from the receiver to a resistive load is demonstrated in Figure S8b. Different load resistances (

from $50\,\Omega$ to $1 \times 10^6\,\Omega$) are connected in series to the receiver, when the 1 inch transmitter is driven by a continuous-mode ultrasound at 460 kHz (which is close to the frequency we are interested to harvest energy). As the load resistance increases, the measured output voltage on the resistor shows a rising tendency and saturates at a higher external load. The instantaneous power output of the receiver is also estimated by $(V_{\mathrm{pp}}^2/(4Z_L))$ [2], where V_{pp} is the peak-to-peak output voltage on the resistive load Z_L. The instantaneous power output reaches the maximal at an external load of $325\,\Omega$, which has a good match with the measured impedance magnitude of the receiver $300\,\Omega$ at 460 kHz. The results indicate that the power transfer can be optimal when the impedance between the receiver and the load is matched.

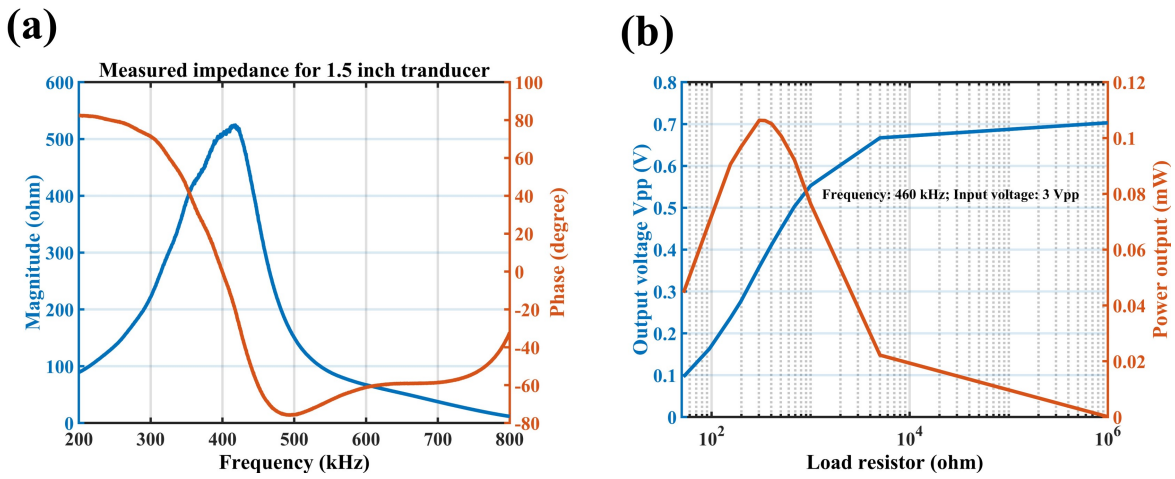

Figure S8: a) The measured impedance of the receiver. b) The output voltage and power from the receiver to a series-connected resistive load, respectively, showing an optimal output power at $325\,\Omega$.

10 Design of the energy harvesting circuit

In this work, a circuit has been designed for energy harvesting. The schematic diagram of the circuit is depicted in Fig. S9. It is implemented on a two-layer printed circuit board (PCB). The traces of the top and bottom layers are shown in Fig. S10(a) and (c), respectively. The 3D rendering of the PCB and a top-view photo are presented in Fig. S10(b) and (d), respectively. As shown in Fig. S10, the PCB can be divided into several functional sections. The top of the PCB houses 9 relays (HUI KE HK19F-DC9V-SHG) that are utilized to switch the wiring for capacitors. Additionally, the middle of the PCB has 10 slots for 220 μF through-hole capacitors. Below the slots is a full bridge rectifier comprising of 4 Schottky diodes (1N5711), and a through-hole red LED is located below the rectifier. The right side of the PCB is equipped with two BNC connectors; the one labeled "INPUT" is connected to the receiving transducer, while the other labeled "OUTPUT" is connected to an oscilloscope. On the left side of the PCB, there is a DC power barrel jack that provides power to the relays. Three switches are located at the bottom left of the PCB. The "SW_WIRING" switch is utilized for switching the wiring of capacitors, the "SW_CHARGE" switch is used for toggling the charging process, and the "SW_LED" switch is used for powering the LED. The designed circuit facilities a more convenient experiment implementation of the energy harvesting compared to existing circuits (e.g., [2]).

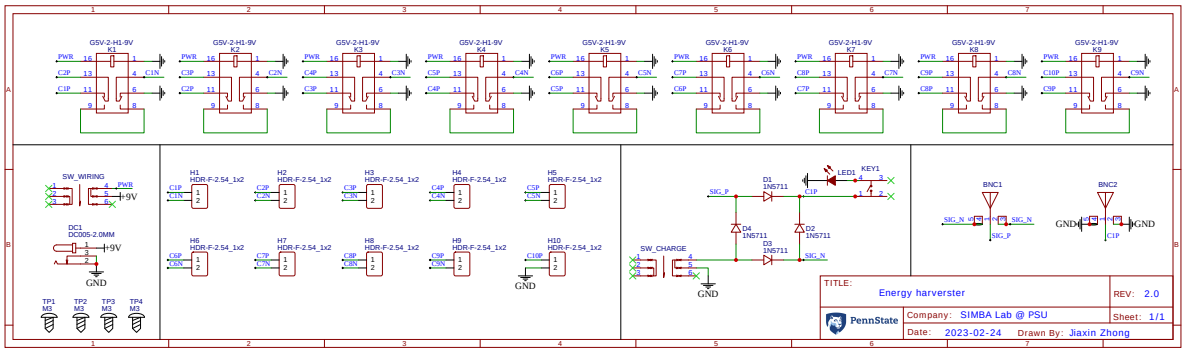

Figure S9: Schematic diagram for the energy harvesting circuit.

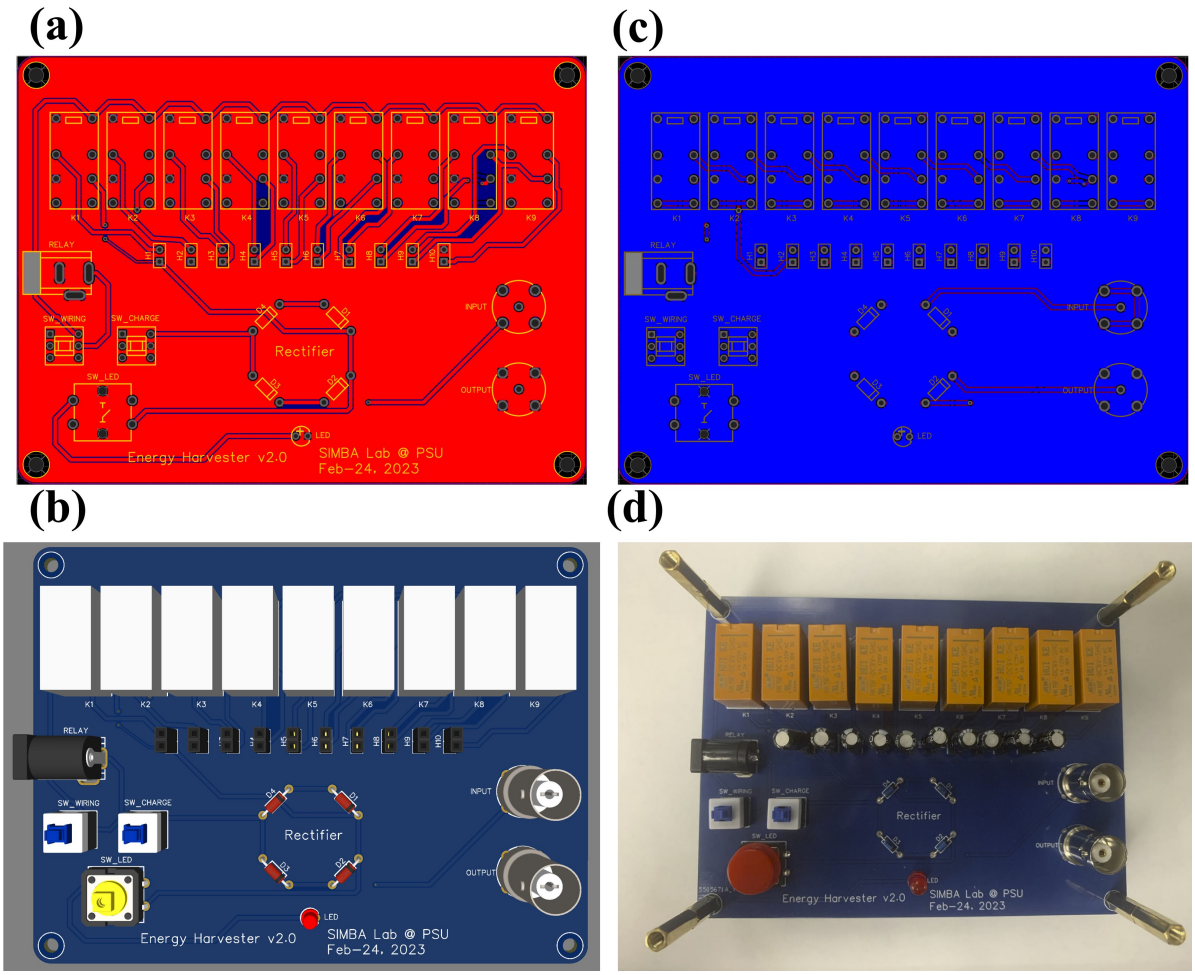

Figure S10: The traces of the circuit on a) the top layer and b) the bottom layer of the PCB. c) 3D rendering and d) the photo of the PCB.

11 The power transmission rate in simulations and measurements

In simulations, the power transmission T is rigorously calculated by the surface integral of acoustic intensity (a default vector variable in COMSOL, $\boldsymbol{I}$ = (acpr.lx,acpr.ly,acpr.lz)) at the transmission side

in COMSOL. The expression for the intensity is,

$$\boldsymbol{I} = \frac{1}{2} Re\left\{p\mathbf{v}^*\right\}$$

We integrate this quantity, for example, along the surface $\boldsymbol{S}$ indicated in Figure S11 for normal and oblique incidence (Please refer to notes S2 and S3 in the supplementary material),

$$T = \int_{\boldsymbol{S}} \boldsymbol{I} d\boldsymbol{S}$$

Consequently, the power transmission rate is $T_{\mathrm{AMM}}/T_{\mathrm{NoPlate}}$ and $T_{\mathrm{NoAMM}}/T_{\mathrm{NoPlate}}$ for "Plate w/ AMM" and "Plate w/o AMM" scenarios, where T_{AMM}, T_{NoAMM} and T_{NoPlate} are the power transmission in the case of "AMM", "No AMM" and "No Plate", respectively.

In measurements (Fig. 3(f) in the manuscript), the power transmission T is approximated by the surface integral of $|p|^2/(2\rho_0 c_0)$ at a plane of $z = 45$mm from the metamaterial plate, which is a reasonable plane-wave approximation (as supported by the pressure distribution shown in Figs. 4(c) and 4(d)) when transitioning to the far field. The power transmission rate is then calculated using $T_{\mathrm{AMM}}/T_{\mathrm{NoPlate}}$ and $T_{\mathrm{NoAMM}}/T_{\mathrm{NoPlate}}$ for "Plate w/ AMM" and "Plate w/o AMM" scenarios. Two observations support our approximation. First, the measured pressure field is very similar to the simulated field in both x-y plane and x-z plane, both of which indicate the far field transition around $z = 45$mm as we calculated in Fig. 3(e). Second, the approximated power transmission rate (using $\int_{z=45\mathrm{mm}} \frac{|p|^2}{2\rho_0 c_0}\,\mathrm{d}S$) has a good agreement with the exact power transmission rate (using $\int_{z=45\mathrm{mm}} \mathrm{acpr.lz}\,\mathrm{d}S$ in COMSOL) in simulation as shown in Figure S12. Consequently, it is reasonable to approximate the power transmission rate in experiments by using the formula,

$$\int_{z=45\mathrm{mm}} \frac{|p|^2}{2\rho_0 c_0}\,\mathrm{d}S$$

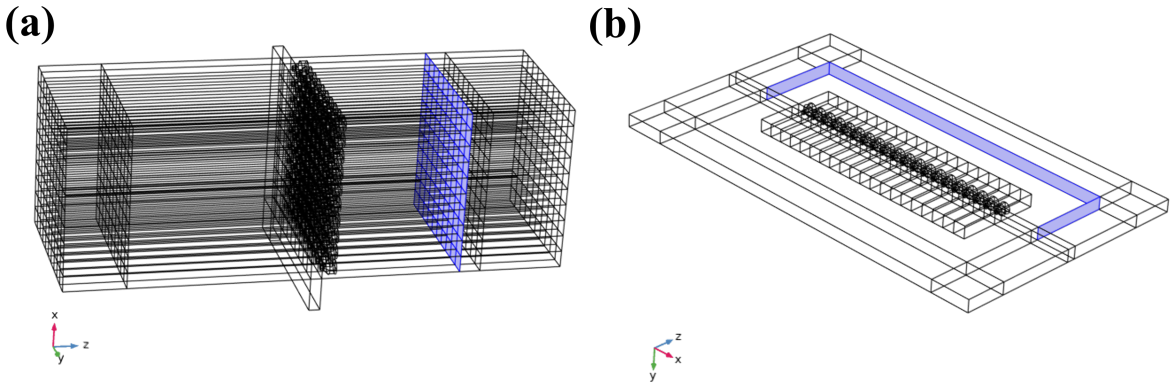

Figure S11: The surface (highlighted in blue) on which the integral of acoustic intensity is conducted for a)the evaluation of the number of unit cell in Note S2 with 20×20 units, b)the evaluation of the incident angle in Note S3.

12 The surface impedance analysis

The homogenization theory [3, 4], which uses effective material parameters to characterize acoustic metamaterials with sub-wavelength unit cells, loses its effectiveness for our unit cell with dimensions around the working wavelength($p \approx 0.46\lambda_0$ and the height is around $0.7\lambda_0$). To demonstrate how the pillars change the impedance of the metallic plate, the surface impedance Z_{surf} at the surface of

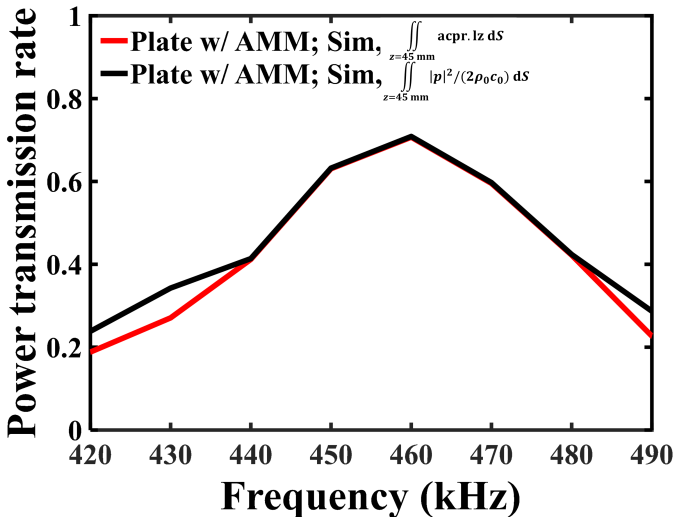

Figure S12: Two methods in COMSOL to calculate the power transmission rate in the case of "Plate w/ AMM". The proposed approximation using $\int_{z=45\text{mm}} \frac{|p|^2}{2\rho_0 c_0}\,\mathrm{d}S$, and the exact method using $\int_{z=45\text{mm}} \text{acpr.lz}\,\mathrm{d}S$). A good agreement between two methods shows that the approximation is reasonable in simulation.

the metallic plate, where the incident wave impinges perpendicularly ($\theta = 0°, \phi = 0°$), is probed in COMSOL by the average of the acoustic pressure divided by the average of the normal acoustic velocity, as shown in Figure S13a. The normalized surface impedance gets closer to 1 around 460 kHz. The power reflection coefficient can be reconstructed from the normalized surface impedance $z_{\text{surf}} = Z_{\text{surf}}/(\rho_0 c_0)$ as $R = |\frac{z_{\text{surf}}-1}{z_{\text{surf}}+1}|^2$. Consequently, the power transmission is $T = 1 - R$, since the loss is negligible as shown in Note S1. Figure S13b shows a good agreement between the recontacted transmission and the actual transmission(probed using a default variable acpr.lz), which confirms the validation of the surface impedance method.

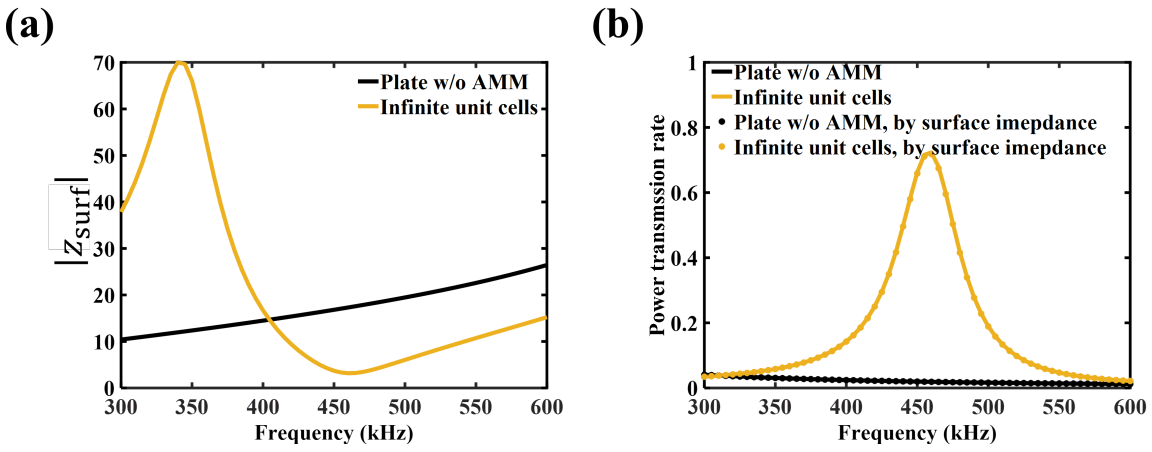

Figure S13: a)The surface impedance Z_{surf} at the surface of the metallic plate, where the incident wave impinges perpendicularly ($\theta = 0°, \phi = 0°$), is probed in COMSOL by the average of the acoustic pressure divided by the average of the normal acoustic velocity. b)The power transmission rate that is probed using a default variable acpr.lz in COMSOL(solid lines) and reconstructed by the surface impedance(dot markers).

References

[1] Lawrence E Kinsler, Austin R Frey, Alan B Coppens, and James V Sanders. *Fundamentals of acoustics*. John wiley & sons, 2000.

[2] Laiming Jiang, Yang Yang, Ruimin Chen, Gengxi Lu, Runze Li, Jie Xing, K Kirk Shung, Mark S Humayun, Jianguo Zhu, Yong Chen, et al. Ultrasound-induced wireless energy harvesting for potential retinal electrical stimulation application. *Advanced Functional Materials*, 29(33):1902522, 2019.

[3] Bogdan-Ioan Popa and Steven A Cummer. Design and characterization of broadband acoustic composite metamaterials. *Physical Review B*, 80(17):174303, 2009.

[4] Vladimir Fokin, Muralidhar Ambati, Cheng Sun, and Xiang Zhang. Method for retrieving effective properties of locally resonant acoustic metamaterials. *Physical review B*, 76(14):144302, 2007.